JOURNAL OF AIRCRAFT
Vol. 32, No. 4, July–August 1995

Computation of a Controlled Store Separation from a Cavity

Christopher A. Atwood*
NASA Ames Research Center, Moffett Field, California 94035-1000

Coupling of the Reynolds-averaged Navier–Stokes equations, rigid-body dynamics, and a pitch-attitude control law is demonstrated in two and three dimensions. The application problem was the separation of a canard-controlled store from an open-flow rectangular cavity at a freestream Mach number of 1.2. The transient flowfield was computed using a diagonal scheme in an overset mesh framework, with the resultant aerodynamic loads used as the forcing functions in the nonlinear dynamics equations. The proportional and rate gyro sensitivities were computed via pole placement techniques for the linearized dynamical equations, in which computed aerodynamic stability derivatives were used. In two dimensions, a comparison between full and linearized flow equations for a perturbed pinned missile was made, and a controlled store was found to possess improved separation characteristics over a canard-fixed store. In three dimensions, trajectory comparisons with quasisteady wind-tunnel data for the canard-fixed case were made. Comparisons of canard-fixed and canard-active simulations showed that controlled store offers only modest improvements in cavity separation characteristics for these high-ejection rate cases.

Nomenclature

C_m = pitching moment coefficient
C_z = normal force coefficient
c = speed of sound
D = cavity depth
$\tilde{F}$ = force, nondimensionalized by $\rho c^2 L^2$
I = body inertia
K_a = proportional gain
K_r = rate gyro sensitivity
L = characteristic length
M = Mach number
$\tilde{M}$ = moment, nondimensionalized by $\rho c^2 L^3$
m = body mass or stage number
Re = Reynolds number
s = Laplace operator
t = time
α = angle of attack
δ = effector deflection angle
ζ = damping ratio
θ = body attitude
ρ = density
τ = canard servocharacteristic time
ω = angular velocity, frequency, or vorticity
$\dot{}$ = time derivative

Subscripts
c = commanded, canard
n = natural
t = tail
∞ = freestream quantity

Superscript
n = time level

Introduction

THE design of current high-performance aircraft has typically been compartmentalized by discipline, most commonly structures, fluids, and controls. However, as the performance demands escalate, aircraft systems have become increasingly interrelated.[1,2] Therefore, there is a need to investigate the optimization of the aircraft in its entirety, not simply by evaluation of its subsystems.

This type of multidisciplinary analysis is currently accomplished with simplified physical models, such as panel flow and modal structural codes. However, in critical regions of the flight envelope these linear methods may fail, leading to the requirement for higher-order models.[3,4] Unfortunately, this increased physical fidelity comes at a high computational price, and hence, fewer design cycles are permitted as compared to the linear methods.

Nonetheless, the simulation of the nonlinear interaction of fluids and rigid body motion will be useful in several ways. First, the simulation could be used to computationally prototype a conventionally designed control system in a nonlinear environment. The simplifications that are typically used to compute the aerodynamic interactions and loads for control law design will not be present in a Navier–Stokes simulation. Second, the coupled simulations could be used to help develop a control law where nonlinear effects are important, using the computed aerodynamic forces and moments instead of tabulated empirical relationships.[5] Hence, computational prototyping and design of an aircraft control system offers a means of reducing aircraft design cycle cost while enhancing safety and performance.

The effort documented here begins to address the interaction of the disciplines of fluids, rigid body dynamics, and controls in nonlinear flight regimes. In order to assess the accuracy of these initial computations, a problem that could be compared against analytic and experimental results was chosen: the cavity store separation problem. A recent wind-tunnel study of the separation of stores from cavity bays were used as a basis for comparison.[6] These quasisteady sting-mounted missile release tests determined the trajectory of an uncontrolled missile from a rectangular cavity and were used to validate the canard-fixed computation.

Previous computational efforts have shown that the component problems of cavity flows[7–9] and uncontrolled store separation[10–13] can be solved with reasonable accuracy using overset grid methods. Tetrahedral cell meshes have also been used to obtain inviscid solutions to specified trajectory problems.[14,15] Here, the combined problem of viscous flow, rigid-body dynamics, and automatic control techniques is addressed using an overset mesh framework.

Received Jan. 3, 1994; presented as Paper 94-0031 at the AIAA 32nd Aerospace Sciences Meeting and Exhibit, Reno, NV, Jan. 10–13, 1994; revision received September 30, 1994; accepted for publication Feb. 20, 1995.

*Research Scientist, Overset Methods. Member AIAA.

The following sections discuss the approach used to solve the coupled system and the results obtained for several two- and three-dimensional cases. Comparisons of numerical results are made against linearized or experimental results as available.

Approach

Figure 1 summarizes the procedure used to solve this series of coupled fluids, body dynamics, and control problems. The solution process begins with the specification of the geometry in the initial grid via the generation of a blocked mesh system. After establishing the initial grid connectivity information, the solution of the flowfield can begin. Depending on the problem being addressed, this fixed grid solution may be steady or possess a bounded envelope. After convergence of this fixed-geometry flow solution, the motion of the body commences.

Computation of the body motion begins by passing the body state and integrated loads to the six-degrees-of-freedom rigid-body dynamics code. The body position and attitude are then integrated one time step and kinematic constraints are applied. The controller then uses the updated body state to compute new effector settings, when are then applied to all effector-attached grids. Finally, since the grids have changed relative positions, the intergrid communication is re-established. This cycle repeats for each time step until the simulation is complete.

Flow Solver

For these simulations the flowfield was computed using the Reynolds-averaged Navier–Stokes (RANS) equations, where the slowly time-varying flow is resolved and rapid fluctuations are modeled. The implicit diagonal scheme of Pulliam and Chaussee[16] was used, implemented in the chimera grid framework of Benek et al.[17] Euler implicit time marching and central second-order spatial differencing was used, with viscous wall conditions specified as no-slip, zero normal pressure gradient, and adiabatic. Information transfer across overset mesh boundaries was implemented using trilinear interpolation of the dependent variable vector, $Q = [\rho, \rho u, \rho v, \rho w, e]^T$. The speed of the flow solver was 13 μs/cell/step on a Cray Y-MP processor.

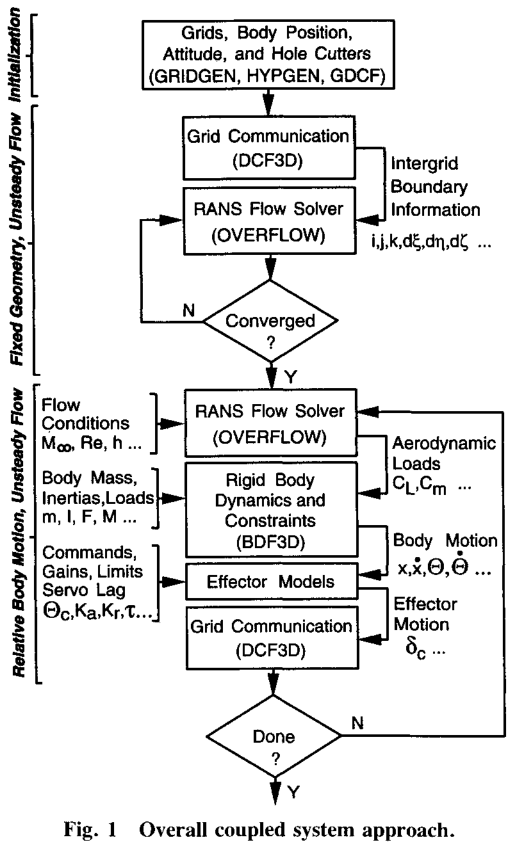

Fig. 1 Overall coupled system approach.

Turbulence Model

The Baldwin-Lomax algebraic turbulence model,[18] as implemented by Buning,[19] was used for the wall-bounded flows with the addition of a variable F_{max} cutoff. Grid topology is chosen such that a unique wall distance is readily available.

The cavity spanning shear layer uses an eddy viscosity obtained using $F(y) = y|\omega|$, as suggested by Baldwin and Lomax for wake regions. Using this suggestion along with Görtler's shear layer solution and the Prandtl mixing length assumption, the model can be modified for application to shear regions.[19] The resultant model has been used successfully in studies of free shear layers, a backward-facing step, and two- and three-dimensional resonant and quieted cavities.[9]

Grid Generation and Communication

The missile and cavity geometries were represented using hyperbolic[20] and algebraic[21] grid generation methods. Generally, the hyperbolic scheme, which solves equations for cell volumes and orthogonality, was used for the wall-bounded regions, while transfinite interpolation was used in shear regions. This topology also leads to straightforward specification of the turbulent regions and allows for the grid refinement of each independent zone. In addition, this type of grid system also permits the reuse of meshes for stability derivative and configuration studies.

The exchange of flow information is accomplished using a domain connectivity function, with the donor-receiver relationship established at each time step using an efficient technique.[22] Although the cost of re-establishing intergrid communication is problem-dependent, the computational expense is generally a third of that used by the diagonalized flow solver. The initial location for the hole-cutters was specified using a graphical interface,[23] after which the movement of the grids and hole-cutters were updated automatically. An example of the overset mesh topology used is shown in Fig. 2, which shows a two-dimensional store configuration at an instant in the separation process.

Kinematics and Rigid-Body Dynamics

The rotational dynamics, outlined in detail elsewhere,[24] are described by Euler's equations of motion that align the xyz coordinates with the body principal axes at the c.g. The body attitude is updated using Euler parameters, which circumvents the gimbal lock problem. For instance, for a rotation θ about an axis λ, Euler parameters can be specified as

$$\varepsilon = [\lambda_1 \sin(\theta/2), \lambda_2 \sin(\theta/2), \lambda_3 \sin(\theta/2), \cos(\theta/2)]^T$$

These Euler parameters, integrated according to the rotational body dynamics, are updated and stored for each grid.[11,22]

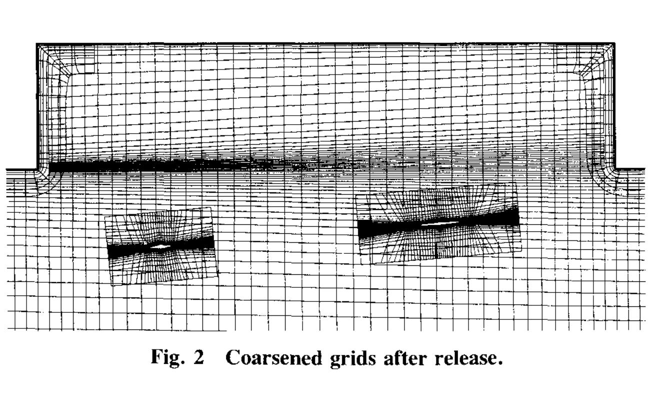

Fig. 2 Coarsened grids after release.

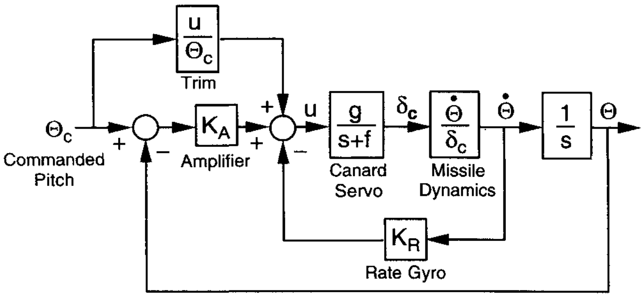

Fig. 3 Block diagram for pitch-attitude missile control system.

Kinematic constraints can be imposed during restricted degree-of-freedom simulations, e.g., the forced ejection process. In addition, the assumption of rigid-body dynamics eliminates the need to store the component grids for all time, since the Euler parameters may be used to compute grid attitude from the initial position.

While the dynamics equations are solved in inertial coordinates, the control laws are typically implemented in a body-fixed coordinate system. Rotating aerodynamic effectors were implemented by summing the commanded effector and body angular velocities ω. Integration of ω gives the proper effector attitude relative to the initial grid positions. The hinge line location is updated according to the attitude of the body. Storage of the hinge line and Euler parameters associated with each grid allows nesting of parent–child bodies to an arbitrary level without modification to the grid communication and support software.

Pitch-Attitude Control Law

The fourth-order state-feedback system shown in Fig. 3 was used as the model for both the two- and three-dimensional missile cases. In Fig. 3 the plant and servo can be approximated by

$$\frac{\dot{\theta}}{\delta_c} = \frac{ds + e}{as^2 + bs + c}, \qquad f = g = \frac{1}{\tau}$$

where $c/a = \omega_n^2$, $b/a = 2\zeta\omega_n$, the servo-time constant was taken as $\tau = 1/75$ s, and d and e are dependent upon body properties and flight conditions. The plant coefficients were determined from the governing equation; they are composed of geometric and flow information as well as the stability derivatives. The stability derivatives were determined from linearized supersonic airfoil theory in the two-dimensional cases and from direct solution of the RANS equations in three dimensions. Pole placement techniques and linearized system time response were used to determine the proportional K_a and the rate gyro K_r sensitivities.

Results

The method outlined above was applied in two dimensions to a perturbed pitch-free case, with comparisons to linearized analysis. In two and three dimensions, solutions to three-degrees-of-freedom cavity store separation problems were determined. In all cases both uncontrolled and controlled cases were computed for comparison.

One-Degree-of-Freedom Simulation

In order to provide some measure of validation, a two-dimensional, one-degree-of-freedom simulation was implemented at a flight altitude of 45,000 ft. Comparison of the linearized and the coupled nonlinear system response for a small perturbation allowed assessment of the basic methodology.

Linearized Dynamics

The equation of motion used, $M_y = I_{yy}\ddot{\theta}$, after neglecting the pitch-damping term, was

$$M_y = q_\infty\{[(C_{l_\alpha}Sd)_c - (C_{l_\alpha}Sd)_t]\theta + (C_{l_\alpha}Sd\delta)_c\}$$

where the body was pinned at the location of the c.g. with distance d from the lifting surface.

Expressing the system in a state variable representation, with $x = [\int \theta, \theta, \dot{\theta}, \delta_c]^T$, then the open-loop equation can be expressed as $\dot{x} = Ax + Bu$, where $u = Qx + Rr$ and r is the commanded state. The closed-loop equation is expressed as

$$\dot{x} = Ax + B[Qx + Rr] = [A + BQ]x + K_aBr$$

$$A + BQ = \begin{bmatrix} 0 & 1 & 0 & 0 \\ 0 & 0 & 1 & 0 \\ 0 & -(c/a) & -(b/a) & d/a \\ -(eg/d)K_a & -g[K_a + (e/d)K_r] & -gK_r & -f \end{bmatrix}$$

$$K_aB = [0, 0, 0, (K_a + K_t)g]^T$$

The state can be computed using Euler explicit integration

$$x^{n+1} = \Delta t\{[A + BQ + (I/\Delta t)]x^n + K_aBr^n\}$$

The gain levels, $K_a = 1.2$, $K_r = 0.06$ s, and $K_t = 1.1$, were computed using root locus and time-domain response. These gains were input into a linearized one-degree-of-freedom dynamics routine to verify implementation of the control law. The solution was initialized with a perturbation in pitch:

$$\theta = \min\left[\delta|_{\text{stall}}, \frac{\delta_{\text{limit}}}{2}\left(1 - \cos\frac{2\pi t}{T}\right)\right]$$

where $\delta_{\text{stall}} = 9$ deg and $T = 0.03$. Figure 4 shows the result of the linearized analysis. A slightly divergent envelope is seen for the canard-fixed case, and damped behavior for the closed-loop system.

For these linearized simulations, a left curve slope of $C_{l_\alpha}|_t = 4\alpha/\sqrt{M_\infty^2 - 1}$ was used for the tail fin, 88% of that slope for the thick canard foil that also stalled at $\alpha = 9$ deg. Com-

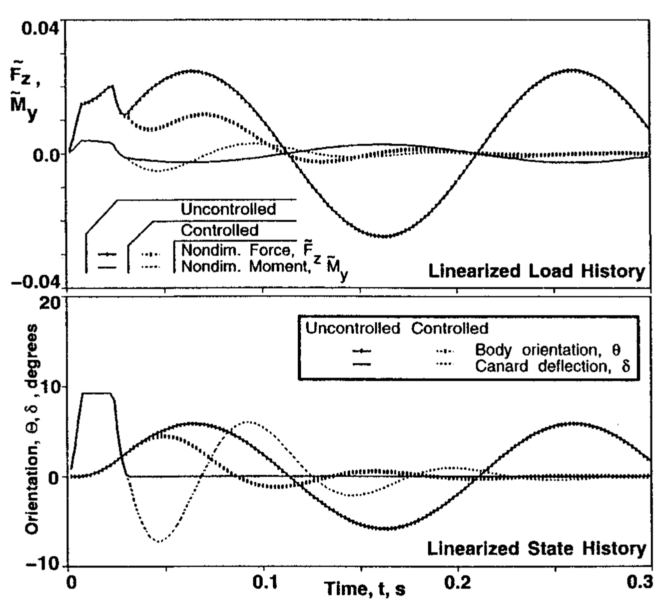

Fig. 4 Linearized two-dimensional missile: body loads, orientation, and canard deflection time histories for both uncontrolled and controlled cases.

parison of the steady lift curves generated by linearized thin airfoil theory and the RANS equations showed that the 4.5% thick tail fin fillows linearized thin airfoil theory at low angles of attack, while the slope of the 15% thick canard foil was about half of $4\alpha/\sqrt{M_\infty^2 - 1}$.

Nonlinear Coupled Simulation

The control law developing previously was also implemented into the code that coupled the RANS equations with rigid-body dynamics. From Fig. 3, the control law can be expressed as

$$\delta_c = g/(s + f)[K_a(\theta_c - \theta) - K_r\dot{\theta} + K_t\theta_c]$$

and integrated using Euler implicit integration

$$\delta_c^{n+1} = [g\Delta t/(f\Delta t + 1)]\{[K_a(\theta_c - \theta^n) - K_r\dot{\theta}^n + K_t\theta_c] + (\delta_c^n/g\Delta t)\}$$

which can then be subjected to limit constraints. The result of the nonlinear solution is shown in Fig. 5 for both canard-fixed and controlled cases. After convergence to a steady-state solution, an accuracy-limited time step size of 46 μs was used, with a computational cost of five Cray Y-MP CPU hours. Grid communication was approximately one-third of the overall CPU time. Figure 5 shows behavior similar to the linearized cases, again with a modestly growing envelope for the canard-fixed case, and damped oscillations for the controlled case. This comparison provides a degree of validation of the implementation of the control law in the coupled code.

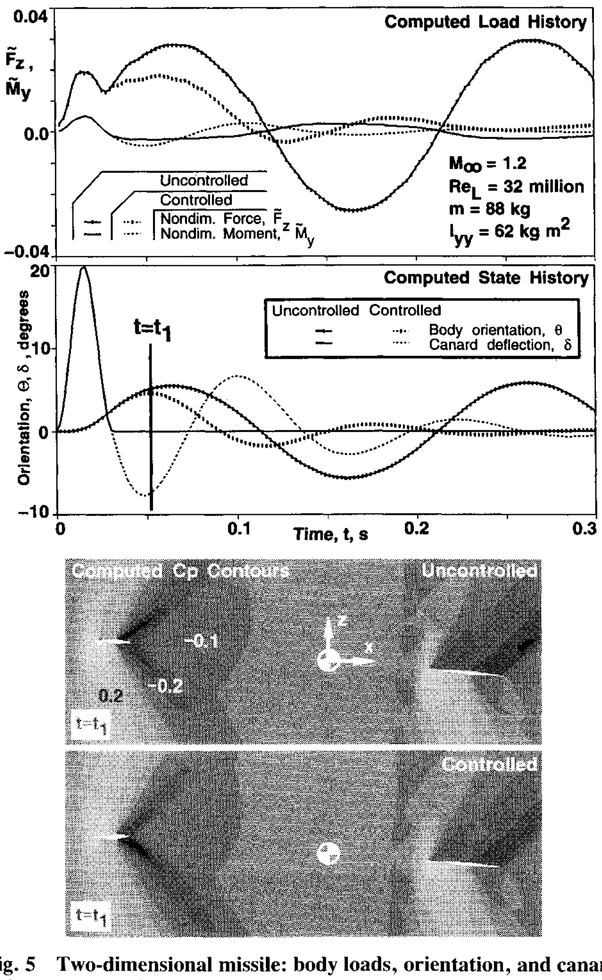

Fig. 5 Two-dimensional missile: body loads, orientation, and canard deflection time histories and instantaneous C_p contours for both uncontrolled and controlled cases at $t = t_1$.

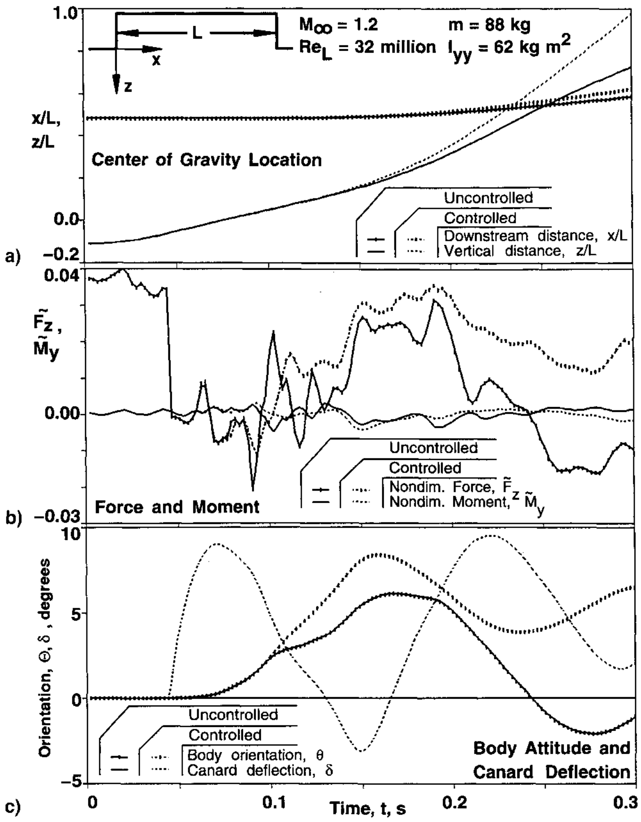

Fig. 6 Two-dimensional controlled store separation: time histories of a) c.g., b) nondimensionalized force and moment, and c) body attitude and canard deflection angles.

Two-Dimensional Controlled Store Separation

Using the control law developed for the one-degree-of-freedom simulation discussed previously, albeit with an arbitrarily chosen $\theta_c = 5$ deg, a three-degrees-of-freedom simulation of a store separating from a cavity was implemented. The separation began with the application of an 18,000-N ejection force for 0.044 s, with corresponding acceleration of about 20 g, during which the controller was off and no angular velocity was imparted to the store, as can be seen in Fig. 6. The solution was initialized with the store fixed in carriage position, allowing damping of the starting numerical transients. Following convergence of the cavity acoustic envelope, the same accuracy-limited time step size of 46 μs was used. The time step size was chosen such that the streamwise Courant number was about unity in the shear layer. This restriction is equivalent to allowing an acoustic wave to propagate only one cell in a single step. Ten grids were used for this 1.3×10^5 point domain. The results, shown in Figs. 6 and 7, show that the nose of the controlled store remains pointed away from the parent body, while the canard-fixed store is pointed towards the parent 0.3 s after release. Also, from Fig. 6a, since the controlled store is commanded to point away from the parent, the separation is faster for the controlled case than for the canard-fixed store, albeit with additional drag. Inspection of the normal force history in Fig. 6b shows a component at about 50 Hz, corresponding to the second stage of Rossiter's formula,[25] which does not significantly excite the body dynamics. In addition, Fig. 6b shows that the uncontrolled store has a net aerodynamic force acting towards the cavity at $t = 0.3$ s.

Three-Dimensional Missile Stability Derivatives

In order to determine the proper feedback gains, the stability derivatives of the missile were computed via the RANS equations. For this three-degrees-of-freedom simulation this

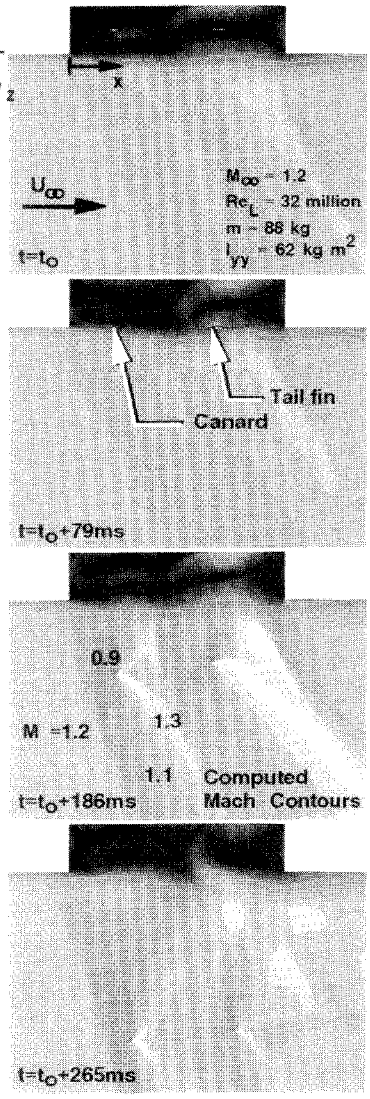

Fig. 7 **Two-dimensional control store separation: instantaneous Mach contours.**

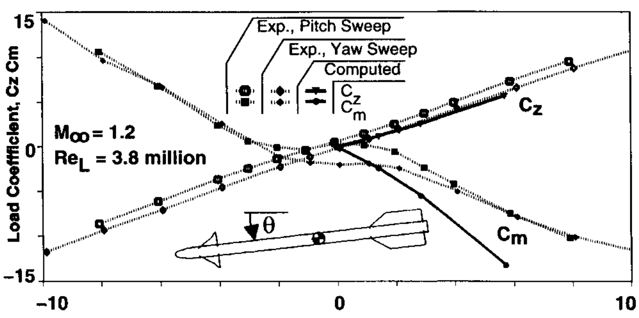

Fig. 8 **Three-dimensional missile: computed and measured normal force and pitching moment coefficients.**

includes C_{m_α}, $C_{m_{\delta_c}}$, and C_{m_q}. These parameters were computed from four steady cases: a nominal $\theta = \delta_c = 0$, a fixed pitch attitude $\theta = 0.1$ rad, $\delta_c = 0$, a fixed canard deflection $\theta = 0$, $\delta_c = 0.1$ rad, and a constant pitch rate $\dot{\theta} = 0.3$ rad/s. Canard motion was permitted by 1/16-in. (full-scale) nominal gap between the missile body and canard. This is a similar arrangement to the actual missile, albeit without the connector pin in the numerical model. The force and moment history was converged to three digits for all integrated loads, requiring approximately 3000 steps, on this 15 grid domain containing 1.5 million points.

Figure 8 compares computed lift and moment curves against experimental data.[6] The differences between the pitch and yaw sweep data may indicate the presence of experimental model asymmetry. Figure 8 shows that while the lift curves are in reasonable agreement, the computed moment curves do not show the inflection at $\theta = 0$ deg seen in the experimental data. The inflection, caused by the canard downwash on the tailfins, is lost in the simulation due to grid coarseness. The computed coefficient of pitching moment due to angle of attack and canard deflection were $C_{m_\alpha} = -132$/rad and $C_{m_{\delta_c}} = 241$/rad. Computed and reported pitch damping coefficients C_{m_q} were, respectively, $-11{,}040$/rad and -5781/rad. Using the computed stability derivatives, gain levels of $K_a = 1.25$, $K_r = 0.13$ s, and $K_t = 0.6$ were chosen, again using both root locus and pinned-missile time domain response.

Three-Dimensional Cavity Store Separation

The modeled geometry for the cavity store separation case can be seen in Fig. 9, which shows the missile at an instant during the trajectory. The domain contains about 2.2 million points distributed in 21 grids, with the body-fixed grids being reused from the previous stability derivative study. Grid communication CPU costs were 20% of the flow solver cost for these three-dimensional cases, and a stability-limited time step of 41 μs was used. Figure 10 shows instantaneous Mach contours from the controlled store separation case, where $t = 0$ is the time at which the ejection loads of 18,204 N and 1391 N-m were applied to the store. Defining a characteristic time T_c to be the elapsed time for a particle to convect across the aperture at the mean shear layer speed, the ejection process was begun $2T_c$ after the artificial starting transients dissipated.

A comparison of the trajectories for both uncontrolled and canard-controlled, with $\theta_c = 10$ deg, cases are shown in Figs. 11a and 11b. The ejection forces were applied to the store such that the velocity at the end of the 8-in. piston stroke was 30 ft/s normal to the cavity with a pitchdown rate of 1 rad/s, not accounting for aerodynamic loads. These rates match the nominal conditions used during wind-tunnel testing. An end-of-stroke rate mismatch owning to the neglection of aerodynamic loads in the computation of ejection force and moments was 1 ft/s and 0.1 rad/s. Comparison of the body attitude curves at $t = 0.044$ s in Fig. 11b shows that no rotation of the store was permitted during the ejection period of the experiment, and that an end-of-stroke rotation of 1 rad/s was instantaneously applied at 0.044 s. These simulations applied a realistic constant force and moment for the duration of the ejection period. Figure 11b also shows that the resultant attitude mismatch at the end-of-stroke was 1.2 deg.

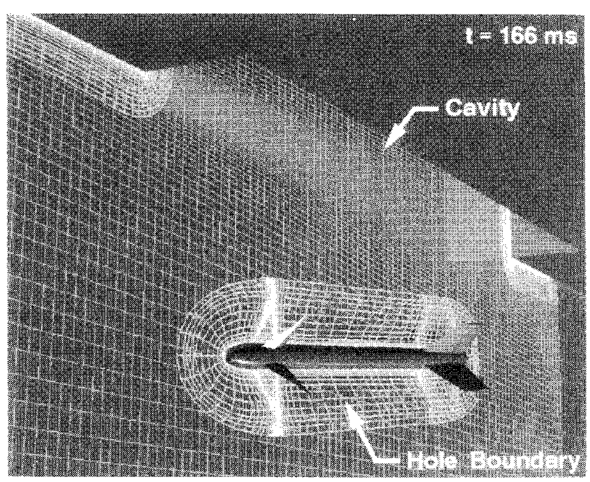

Fig. 9 **Three-dimensional uncontrolled store: geometry and coarsened symmetry plane grids for canard-fixed missile in release.**

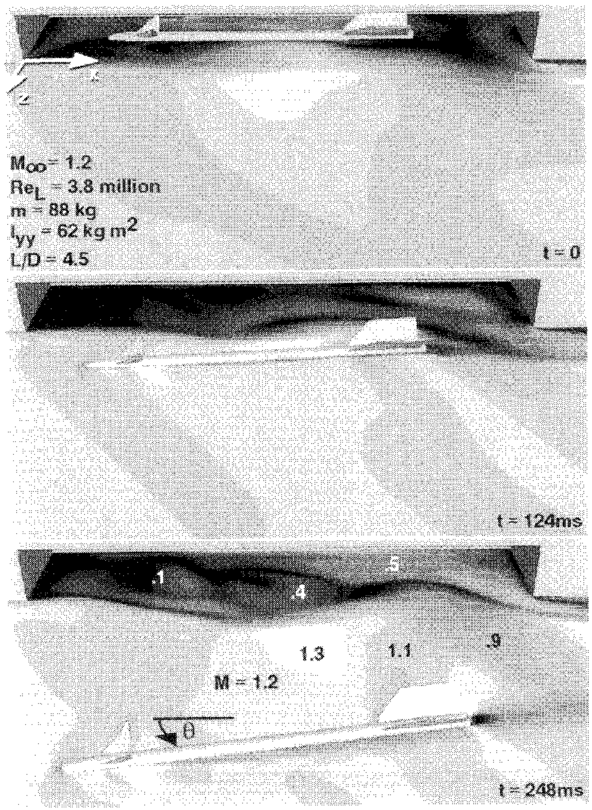

Fig. 10 Three-dimensional controlled store: instantaneous Mach contours on the symmetry plane.

Comparison of the linear trajectories in Fig. 11b for the experiment and the fin-fixed store case shows reasonable for the vertical motion, but less drag acting on the simulated store as compared to the sting-mounted store experiment. Inspection of the vertical position curves at $t = 0.3$ s in Fig. 11b also shows that only slightly improved separation distance is achieved by the controlled store over the canard-fixed case for this fast ejection case.

The store attitude from experimental and canard-fixed computational results are compared in Fig. 11b, which shows a difference of 2 deg by the end of the simulation. This discrepancy may be attributable to the time-averaging of the experimental loads, sting effects not included in the computation, numerical errors, or differences in the treatment of ejection process.

Figure 11b also compares the attitude of the canard-active store with the canard-fixed case. The attitude of the controlled store approaches the commanded value smoothly, with canard deflections of less than 7 deg controlling the body attitude and angular velocity. At the end of the simulation, the attitude of the controlled store is about 10 deg, which is the commanded attitude, and is nearly trimmed in moment (see Fig. 11c). In addition, the body attitude for both canard-fixed and active cases were seen to contain a small 50-Hz component, implying that the missile is dynamically responding to the second stage of cavity feedback. This effect may be indirectly noted by the oscillations in δ seen in Fig. 11b.

Aerodynamic forces and moments are shown in Fig. 11c, where the experimental load histories were time-averaged over 1.0 s from samples every 0.01 s during the quasisteady wind-tunnel test. Comparison of the experimental and simulated loads for the canard-fixed missile show similar trends, with the negative (restoring) moment and positive force evident from 200 to 300 ms. The store loads show a strong component at the second stage of cavity oscillation, with the maximum fluctuating component reached as the store was traversing the shear layer, from 50 to 150 ms.

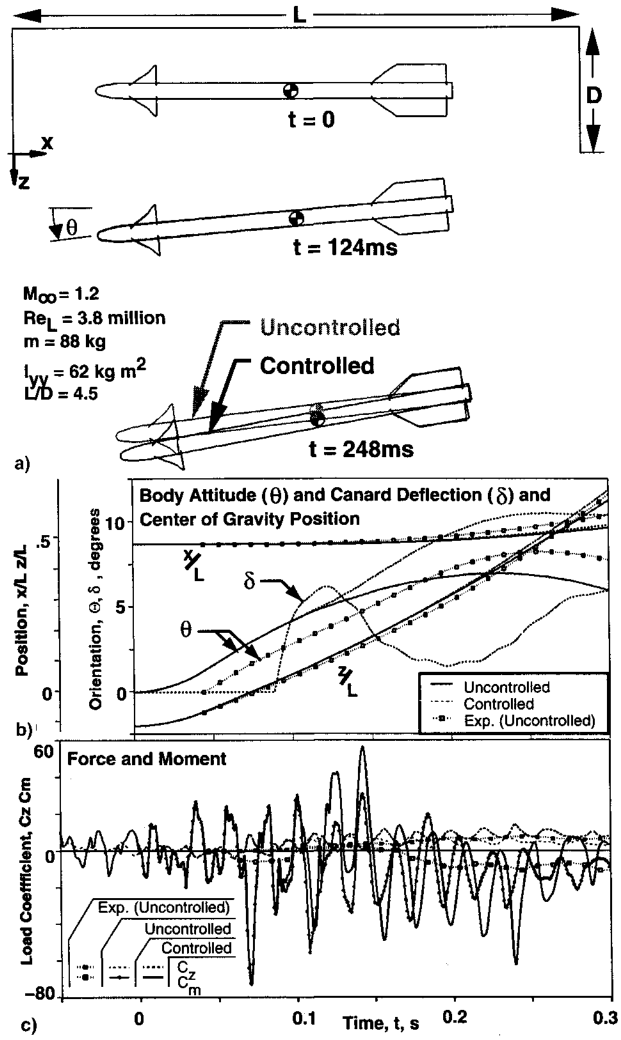

Fig. 11 Three-dimensional store separation: comparison of trajectories and load histories.

Figure 11c also shows that the controlled simulation generally possesses higher fluctuating loads and a phase lag as compared to the uncontrolled simulation. In addition, it may be seen from Fig. 11c that the fluctuating load levels drop at $t = 250$ ms, about the same time as the canards pierce the shock attached to the leading edge of the cavity (see Fig. 10). These complex time-dependent effects would generally not be seen from lower-order fluid models. Finally, the controlled store can be seen to be approaching a trimmed state by inspection of the pitching moment from 250 to 300 ms.

Conclusions

A state-feedback pitch attitude control law has been implemented in a coupled Reynolds-averaged Navier–Stokes/rigid-body dynamics code. The coding methodology of the effector kinematics will allow rapid implementation of arbitrarily complex multiple-effector control laws.

Validation of the coupled code was performed in two and three dimensions. For a perturbed two-dimensional canard/tail-fin case, the nonlinear and linearized results showed good comparison with the controller either active or off. However, comparison of a three-dimensional canard-fixed computation with quasisteady wind-tunnel results showed some differences in streamwise position and pitch orientation.

Application of the control law to both two- and three-dimensional, three-degrees-of-freedom cavity store separation problems revealed improved trajectory characteristics as compared to canard-fixed simulation. However, due to the high ejection rates of the stores, the improvement was modest.

For smaller ejection loads, aerodynamic loads will be relatively more significant, and hence, the improvement in trajectory due to aerodynamic control may be larger. Decreased ejection loads will reduce the incidence of vehicle system failures owing to large accelerations.

Acknowledgments

This investigation was supported by Grants NCC 2-799 under Overset Methods and NCC 2-677 under MCAT Institute. Computations were performed on the Numerical Aerodynamic Simulation (NAS) facility Cray Y-MP and C90, the NASA/Ames Central Computing Facility (CCF) Cray Y-MP, and Silicon Graphics workstations at the Computational Aerosciences Branch. Special thanks to Richard E. Dix, Robert L. Meakin, Kalpana Chawla, and George Meyer for their assistance with the experimental data, software tools, and interpretation of results.

References

[1]Franklin, J. A., Hynes, C. S., Hardy, G. H., Martin, J. L., and Innis, R. C., "Flight Evaluation of Augmented Controls for Approach and Landing of Powered-Lift Aircraft," *Journal of Guidance, Control, and Dynamics*, Vol. 9, No. 5, 1986, pp. 555–565.

[2]Franklin, J. A., Stortz, M. W., and Mihalœw, J. R., "Integrated Flight/Propulsion Control of Supersonic STOVL Aircraft," *International Powered-Lift Conf.* (London), 1990, pp. III9.1–12.

[3]Meyer, G., and Cicolani, L., "Application of Nonlinear System Inverses to Automatic Flight Control Design—System Concepts and Flight Evaluations," AGARDograph 251, July 1981.

[4]Smith, G. A., and Meyer, G., "Aircraft Automatic Flight Control System with Model Inversion," *Control and Dynamics Systems, Advances in Aeronautical Systems*, Vol. 38, Academic, San Diego, CA, 1990.

[5]Tobak, M., and Schiff, L. B., "Aerodynamic Mathematical Modeling—Basic Concepts," AGARD Lecture Series 114 on Dynamic Stability Parameters, Lecture No. 1, March 1981.

[6]Dix, R. E., and Butler, C., "Cavity Aeroacoustics," *Proceedings of the Store Carriage Integration and Release Conference*, Royal Aeronautical Society, Bath, England, UK, 1990, pp. 4.1–4.34.

[7]Atwood, C. A., and Van Dalsem, W. R., "Flowfield Simulation About the Stratospheric Observatory for Infrared Astronomy," *Journal of Aircraft*, Vol. 30, No. 5, 1993, pp. 719–727.

[8]Suhs, N. E., "Transonic Flow Calculations for a Cavity with and Without a Store," Arnold Engineering Development Center, AEDC-TR-92-4, Arnold AFB, TN, Sept. 1992.

[9]Atwood, C. A., "Selected Computations of Transonic Cavity Flows," *Computational Aero- and Hydro-Acoustics, ASME 1993 Fluids Engineering Conference*, FED-Vol. 147, Washington, DC, 1993, pp. 7–18.

[10]Dougherty, F. C., Benek, J. A., and Steger, J. L., "On Applications of Chimera Grid Schemes to Store Separation," NASA TM-88193, Oct. 1985.

[11]Meakin, R. L., "Computations of the Unsteady Flow About a Generic Wing/Pylon/Finned-Store Configuration," AIAA Paper 92-4568, Aug. 1992.

[12]Lijewski, L., and Suhs, N. E., "Chimera-Eagle Store Separation," AIAA Paper 92-4569, Aug. 1992.

[13]Yen, G. W., Newmann, J., and Baysal, O., "Dynamic Overlapped Grid Simulation of Aerodynamically Determined Three-Dimensional Relative Motion," AIAA Paper 93-3018, July 1993.

[14]Löhner, R., "Three-Dimensional Fluid-Structure Interaction Using a Finite Element Solver and Adaptive Remeshing," *Computing Systems in Engineering*, Vol. 1, Nos. 2–4, 1990, pp. 257–272.

[15]Noack, R., and Bishop, D., "A Three-Dimensional Delaunay Unstructured Grid Generator and Flow Solver for Bodies in Relative Motion," AIAA Paper 93-3349, July 1993.

[16]Pulliam, T. H., and Chaussee, D. S., "A Diagonal Form of an Implicit Approximate-Factorization Algorithm," *Journal of Computational Physics*, Vol. 39, Feb. 1981, pp. 347–363.

[17]Benek, J. A., Buning, P. G., and Steger, J. L., "A 3-D Chimera Grid Embedding Technique," AIAA Paper 85-1523, July 1985,

[18]Baldwin, B. S., and Lomax, H., "Thin-Layer Approximation and Algebraic Model for Separated Turbulent Flows," AIAA Paper 78-257, Jan. 1978.

[19]Buning, P. G., and Chan, W. M., "OVERFLOW/F3D User's Manual, Version 1.5," NASA Ames Research Center, Moffett Field, CA, Nov. 1990.

[20]Chan, W. M., and Steger, J. L., "Enhancements of a Three-Dimensional Hyperbolic Grid Generation Scheme," *Applied Mathematics and Computation*, Vol. 51, 1992, pp. 181–205.

[21]Steinbrenner, J. P., Chawner, J. R., and Fouts, C. L., "A Structured Approach to Interactive Multiple Block Grid Generation," AGARD FDP Specialists Meeting on Mesh Generation for Complex Three-Dimensional Configurations, Loen, Norway, May 1989.

[22]Meakin, R. L., "A New Method for Establishing Inter-Grid Communication Among Systems of Overset Grids," AIAA Paper 91-1586, June 1991.

[23]McCann, K. M., and Meakin, R. L., "GDCF—An Interactive Approach to Domain Connectivity Among Systems of Overset Grids," *AIAA 11th Computational Fluid Dynamics Conference* (Orlando, FL), 1993, pp. 1039, 1040, Paper I (86-LFD-16).

[24]Meakin, R. L., "Overset Grid Methods for Aerodynamic Simulation of Bodies in Relative Motion," 8th Aircraft/Stores Compatibility Symposium, Joint Ordnance Commanders Group Aircraft/Stores Compatibility Subgroup, Fort Walton Beach, FL, Oct. 1990.

[25]Rossiter, J. E., "Wind-Tunnel Experiments on the Flow over Rectangular Cavities at Subsonic and Transonic Speeds," Royal Aircraft Establishment R&M 3438, Oct. 1964.